Monthly Notices
of the
ROYAL ASTRONOMICAL SOCIETY

MNRAS **487,** 3650–3663 (2019)
Advance Access publication 2019 June 05

doi:10.1093/mnras/stz1539

C IV black hole mass measurements with the Australian Dark Energy Survey (OzDES)

J. K. Hoormann,[1★] P. Martini,[2,3★] T. M. Davis,[1★] A. King,[4] C. Lidman,[5] D. Mudd,[6] R. Sharp,[5] N. E. Sommer,[5] B. E. Tucker,[5] Z. Yu,[3] S. Allam,[7] J. Asorey,[8] S. Avila,[9] M. Banerji,[10,11] D. Brooks,[12] E. Buckley-Geer,[7] D. L. Burke,[13,14] J. Calcino,[1] A. Carnero Rosell,[15,16] D. Carollo,[17] M. Carrasco Kind,[18,19] J. Carretero,[20] F. J. Castander,[21,22] M. Childress,[23] J. De Vicente,[15] S. Desai,[24] H. T. Diehl,[7] P. Doel,[12] B. Flaugher,[7] P. Fosalba,[21,22] J. Frieman,[7,25] J. García-Bellido,[26] D. W. Gerdes,[27,28] D. Gruen,[13,14,29] G. Gutierrez,[7] W. G. Hartley,[12,30] S. R. Hinton,[1] D. L. Hollowood,[31] K. Honscheid,[2,32] B. Hoyle,[33,34] D. J. James,[35] E. Krause,[36] K. Kuehn,[37] N. Kuropatkin,[7] G. F. Lewis,[38] M. Lima,[16,39] E. Macaulay,[9] M. A. G. Maia,[16,40] F. Menanteau,[18,19] C. J. Miller,[27,28] R. Miquel,[20,41] A. Möller,[5] A. A. Plazas,[42] A. K. Romer,[43] A. Roodman,[13,14] E. Sanchez,[15] V. Scarpine,[7] M. Schubnell,[28] S. Serrano,[21,22] I. Sevilla-Noarbe,[15] M. Smith,[23] R. C. Smith,[44] M. Soares-Santos,[45] F. Sobreira,[16,46] E. Suchyta,[47] E. Swann,[9] M. E. C. Swanson,[19] G. Tarle,[28] and S. A. Uddin[48] (DES Collaboration)

Affiliations are listed at the end of the paper

Accepted 2019 May 30. Received 2019 May 29; in original form 2019 February 11

ABSTRACT

Black hole mass measurements outside the local Universe are critically important to derive the growth of supermassive black holes over cosmic time, and to study the interplay between black hole growth and galaxy evolution. In this paper, we present two measurements of supermassive black hole masses from reverberation mapping (RM) of the broad C IV emission line. These measurements are based on multiyear photometry and spectroscopy from the Dark Energy Survey Supernova Program (DES-SN) and the Australian Dark Energy Survey (OzDES), which together constitute the OzDES RM Program. The observed reverberation lag between the DES continuum photometry and the OzDES emission line fluxes is measured to be 358^{+126}_{-123} and 343^{+58}_{-84} d for two quasars at redshifts of 1.905 and 2.593, respectively. The corresponding masses of the two supermassive black holes are 4.4×10^9 and 3.3×10^9 $M_\odot$, which are among the highest redshift and highest mass black holes measured to date with RM studies. We use these new measurements to better determine the C IV radius−luminosity relationship for high-luminosity quasars, which is fundamental to many quasar black hole mass estimates and demographic studies.

Key words: accretion, accretion discs – black hole physics – galaxies: evolution – quasars: emission lines.

1 INTRODUCTION

The masses of the supermassive black holes at the centres of galaxies are fundamental measurements for studies of galaxy evolution, active galactic nuclei (AGNs), and the interaction between black hole and galaxy growth over cosmic time. Mass measurements in the local Universe are most often obtained with high-spatial resolution spectroscopy that can resolve the sphere of influence of the black hole (Kormendy & Richstone 1995; Richstone et al. 1998; Ferrarese & Ford 2005; Kormendy & Ho 2013), yet even the largest telescopes lack sufficient angular resolution for such measurements at significant distances.

★ E-mail: j.hoormann@uq.edu.au (JKH); martini.10@osu.edu (PM); tamarad@physics.uq.edu.au (TMD)

Fortunately such measurements are possible for AGNs with broad emission lines, irrespective of distance, through intensive time-domain spectrophotometry. The technique of reverberation mapping (RM) resolves very small scales with measurement of the time lag between variations in the continuum and the broad-line region (Blandford & McKee 1982; Peterson 1993). This provides a measurement of the distance of the broad emission line region (BLR) from the supermassive black hole because the continuum variations originate in the accretion discs on scales of only a few Schwarzschild radii, while the BLR is approximately an order of magnitude or more further away. The time lag, τ, between the continuum variation and when the BLR reverberates in response is consequently a measurement of the size of the BLR: $R_{\rm BLR} = c\tau$. This measurement is combined with a measurement of the characteristic velocity, ΔV, of the BLR as measured by spectral line widths to determine the black hole mass through an application of the virial theorem:

$$M_{\rm BH} = f\frac{R_{\rm BLR}\Delta V^2}{G}. \quad (1)$$

The quantity f is a dimensionless factor that accounts for the geometry, orientation, and kinematics of the BLR.

The factor f has been measured with reverberation-based black hole mass measurements for many nearby galaxies that also have black hole mass estimates from the correlation between black hole mass and the stellar velocity dispersion of the host galaxy spheroid known as the $M_{\rm BH}$–σ_* relationship (Ferrarese & Merritt 2000; Gebhardt et al. 2000a). This relationship has been measured for large numbers of nearby quiescent (Tremaine et al. 2002; McConnell & Ma 2013) and active galaxies (Gebhardt et al. 2000b; Woo et al. 2010; Grier et al. 2013, 2017a). The ensemble average value of f is $\langle f\rangle = 4.47 \pm 1.25$ based on about 30 AGNs with both σ_* and $M_{\rm BH}$ measurements from RM (Woo et al. 2015). This average value for f is also consistent with measurements of two nearby galaxies that both have reverberation-based masses and measurements from spatially resolved kinematics (Davies et al. 2006; Hicks & Malkan 2008; Onken et al. 2014) and sophisticated dynamical models of the BLR (Pancoast, Brewer & Treu 2014; Williams et al. 2018).

Most RM campaigns have targeted variable AGNs in the local Universe ($z < 0.3$) to measure the response of the prominent Hβ line (Kaspi et al. 2000; Peterson & Horne 2004; Bentz et al. 2009; Denney et al. 2010; Grier et al. 2012). These measurements showed that there is a tight relationship between $R_{\rm BLR}$ and the AGN luminosity, the R–L relationship (Bentz et al. 2009). The power-law slope of the relationship is $\alpha = 0.533^{+0.035}_{-0.033}$, which is consistent with the value of 0.5 expected from simple photoionization arguments, and the scatter around this slope is only 0.13 ± 0.02 dex for the best subset of the data (Bentz et al. 2013). The R–L relationship is extraordinarily useful because it provides a way to estimate the black hole mass of an AGN with a single spectroscopic measurement of the Hβ region, rather than the many tens to even a hundred epochs required to measure a reverberation-based mass for a single object (Wandel, Peterson & Malkan 1999; Vestergaard 2002; Vestergaard & Peterson 2006). The small scatter also led to the suggestion that the R–L could be used to treat AGNs as standard candles (Watson et al. 2011). The visibility of luminous AGNs out to higher redshifts than Type Ia supernovae makes them attractive probes of some dark energy models (King et al. 2014).

At higher redshifts, it is either not possible or much more challenging to measure the Hβ emission line. Various studies have consequently used spectroscopic observations of select samples of quasars to produce empirical methods to estimate black hole masses with other broad emission lines, most notably the prominent Mg II and C IV lines (McLure & Jarvis 2002; Vestergaard & Peterson 2006; Wang et al. 2009). These methods typically require extrapolations to higher redshift and higher luminosity AGNs, and are also more uncertain due to differences in the geometry and kinematics of the Mg II and C IV line regions relative to Hβ. This has consequently inspired efforts to directly measure reverberation masses for high-redshift AGNs with these emission lines. These studies have measured masses for 19 AGNs with the C IV line (Peterson et al. 2004, 2005; Metzroth, Onken & Peterson 2006; Kaspi et al. 2007; Trevese et al. 2014; Lira et al. 2018) and 10 with the Mg II line (Clavel et al. 1991; Reichert et al. 1994; Metzroth et al. 2006; Shen et al. 2015), in addition to RM of higher redshift AGNs with the Hβ line (Shen et al. 2016; Grier et al. 2017b). These measurements indicate that Hβ and Mg II emanate at the same radius with C IV originating from the inner regions of the BLR clouds (Kaspi et al. 2007; Trakhtenbrot & Netzer 2012). However, only a few AGNs currently have lags measured using multiple emission lines that are necessary to fully understand the stratification of the BLR.

In this paper, we present some of the first results from the OzDES RM Program (King et al. 2015), which combines spectroscopic observations from the Australian Dark Energy Survey (OzDES, see Yuan et al. 2015; Childress et al. 2017) with photometric data from the Dark Energy Survey (DES, see Flaugher 2005; Dark Energy Survey Collaboration 2016). Section 2 details the observations obtained by OzDES and the data calibration procedures. Section 3 describes our measurements of the emission line fluxes and reverberation lags, and the resultant black hole masses for two high-redshift AGNs. We use these new measurements together with other measurements in the literature to calculate a new C IV R–L relationship in Section 4 and discuss and summarize our results and the outlook to the future in Section 5.

2 OBSERVATIONS

The OzDES RM Program combines spectroscopic observations from the OzDES survey and photometric observations from Dark Energy Survey Supernova Program (DES-SN). DES is conducted with the CTIO 4 m Blanco Telescope using the Dark Energy Camera (DECam Flaugher et al. 2015) in the *grizY* bands. The DES footprint comprises 5000 deg^2 at high galactic latitude that are visible from the Southern hemisphere (Diehl et al. 2016, 2018). The main science goal of DES is to study the expansion of the Universe through four cosmological probes: weak gravitational lensing (Chang et al. 2018), galaxy clustering (Elvin-Poole et al. 2018), baryon acoustic oscillations (Abbott et al. 2018), and supernovae (SN). The first three cosmological probes use data from the wide-area survey. DES-SN uses approximately weekly observations of 10 dedicated SN fields that together comprise approximately 27 deg^2 (Kessler et al. 2015; D'Andrea et al. 2018). After Science Verification in the 2012 semester, DES began in 2013 and completed the wide-area survey in 2019 January (the supernova survey ended in 2017).

OzDES is a spectroscopic follow-up program for the 10 DES-SN fields. The survey is carried out using the AAOmega spectrograph (Smith et al. 2004) and the Two Degree Field (2dF) 400 multi-object fibre positioning system (Lewis et al. 2002), which covers the wavelength range of 3700–8800 Å. The primary goal of OzDES is to obtain redshifts for SN host galaxies (Yuan et al. 2015; Childress et al. 2017). OzDES was awarded 100 nights on the 3.9 m Anglo-Australian Telescope (AAT) that were originally planned over 5 yr. Twelve nights were reallocated from the fourth and fifth season into

a sixth season in 2018B. The purpose of this reallocation was to allow time to measure SN host galaxy redshifts for discoveries that were made at the end of 2017B.

2.1 OzDES reverberation mapping candidates

In addition to supernova host galaxies, the OzDES survey also targets AGNs for the OzDES RM program, as well as a number of other ancillary target classes (Childress et al. 2017). The possible AGN targets in the DES-SN fields were selected based on colour and variability using the data from the DES Year 1 catalogues, DES Y1A1. These targets were spectroscopically confirmed by OzDES (Tie et al. 2017). The OzDES RM sample was chosen based on the presence of clear H β, Mg II, and/or C IV lines with a median SNR in the line greater than 10 as measured from spectra of a larger sample of AGNs that were observed during the first 2 yr of OzDES. To enhance the science output, a lower SNR > 5 threshold was used for AGNs at $z > 3$ and/or for AGNs with more than one broad emission line in the spectral bandpass (King et al. 2015). Additionally, AGNs that had fewer than 10 epochs of photometric observations after the first DES season were removed from the sample. Such AGNs typically were close to or in the DECam CCD gaps (Tie et al. 2017; Mudd et al. 2018). The final OzDES RM sample includes 771 AGNs with $0.1 < z < 4.5$.

An extensive simulation study by King et al. (2015) shows that OzDES will be able to measure time lags for 30−40 per cent of the AGNs once spectroscopic epochs are observed for all six seasons. This success rate is highly dependent on redshift and other factors, such as SNR and the calibration uncertainty. For example, the success rate for the C IV line is expected to be closer to 20–30 per cent (King et al. 2015). At present the first 4 yr of DES photometry have been processed through the DES Data Management System and are available for analysis (Morganson et al. 2018), as well as for calibration of the OzDES spectroscopy . On average these data include about 110 photometric epochs and 15 spectroscopic epochs. Most AGNs have four additional spectroscopic epochs that were obtained during the fifth year of DES, and four additional OzDES observing runs have been completed for Year 6.

2.2 Spectroscopic calibration

The high-quality DES photometry calibration provides good measurements of the continuum flux variations of all of the AGNs in our sample (Burke et al. 2018). Emission line RM also requires measurements of the emission line flux variations from the OzDES spectra. These spectra are obtained with a fibre spectrograph, and consequently the amount of flux in the fibre at each epoch depends on many factors, most notably the image quality, airmass, transparency, and the accuracy of the fibre placement. Furthermore, these factors can impact not just the total flux that enters the fibre at each epoch, but also the wavelength-dependent flux calibration for each epoch. Two wavelength-dependent factors that are important are the variation in image quality (seeing) with wavelength and chromatic effects in the spectrograph optics, where the latter could depend on location in the field of view. A common practice with fibre spectroscopy is to flux-calibrate the spectra with photometric measurements in multiple, broad-band filters. For example, Hopkins et al. (2013) used SDSS photometry to flux-calibrate spectra from the AAOmega spectrograph for the Galaxy And Mass Assembly (GAMA) sample and obtained a typical flux calibration uncertainty of about 10 per cent, although the quality degraded to somewhat poorer than 20 per cent at the extreme ends of the wavelength range.

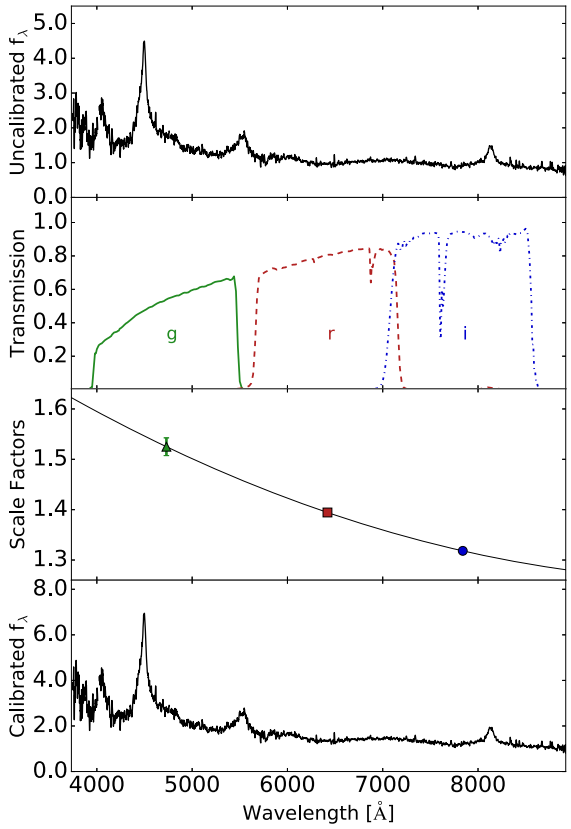

Figure 1. Single smoothed spectrum of the AGN DES J022828.19−040044.30 taken on MJD 56917.615 (*top panel*). We calculate OzDES instrumental magnitudes in the *gri* bands with the DES transmission functions (*second panel*). The scale factors are in units of 10^{-16} erg s^{-1} cm^{-2} Å^{-1} counts^{-1}. We fit a second-order polynominal to these scale factors and use this function to convert the OzDES spectroscopic pipeline output to the fluxes measured from contemporaneous DES photometry (*third panel*). The calibrated spectrum is shown in the bottom panel. The flux is in units of 10^{-16} erg s^{-1} cm^{-2} Å^{-1}.

The variability of AGN precludes the use of a single photometric measurement for flux calibration. Instead we take advantage of the near-weekly cadence of the DES-SN observations, which provide DES photometric measurements in the *griz* filters within a week of the OzDES epochs.[1] We linearly interpolate between the photometric epochs immediately before and after each spectroscopic epoch to estimate the fluxes in the *gri* filters at our spectroscopic epoch. These three bands overlap nearly perfectly with the spectroscopic bandpass. Next, we compute instrumental fluxes in these three bands from the OzDES spectra, fit a second-order polynomial to the flux ratio at the effective wavelength of each bandpass, and use this polynomial to calibrate each OzDES epoch. Fig. 1 shows an example of our approach. The top panel shows a single spectroscopic epoch that was smoothed using an exponential smoothing kernel with a decay factor of 0.9 and search window of 11 pixels. The second panel shows the *gri* photometric bands that overlap the OzDES wavelength range, the third panel shows the ratio of the instrumental and DES flux values, as well as the polynomial fit, and the bottom panel

[1]Occasionally particularly bad or good weather has led to observations of the same fields over multiple nights in a single OzDES run. In these cases, we combine the multiple nights of observations into a single OzDES epoch.

shows the AGN spectrum after the flux calibration. Through the use of Gaussian processes use the measured uncertainties in the scale factors that were dominated by the photometric uncertainty, to determine the wavelength-dependent variance on the calibration model. This variance was added in quadrature with the other sources of uncertainty. This spectrophotometric code is publicly available.[2] The calibration is performed on each individual observation before the data is combined. By coadding the data taken during a given observing run the noise of the spectrum is reduced Childress et al. (2017).

The quality of the spectroscopic flux calibration is critical to our emission line RM program. As noted in the simulation study of King et al. (2015), using the flux calibration uncertainties measured by GAMA would result in many of our emission line light curves being limited more by flux calibration than the signal-to-noise ratio (SNR) of the spectroscopy. We consequently have made numerous improvements to the calibration protocols and software pipeline in order to improve the flux calibration of the OzDES spectra taken at the AAT. These include upgrades to the detectors and additional dome flat-field calibrations that better account for relative wavelength-dependent transmission between fibres. These improvements are described in Yuan et al. (2015) for Year 1 of OzDES and in Childress et al. (2017) for changes through the end of Year 3.

An important part of our calibration strategy is observations of tens of F stars in each field. These F star observations have provided a valuable check on improvements to the calibration and data processing procedures, as well as a convenient way to quantify the calibration uncertainties. Fig. 2 demonstrates one measurement of the calibration uncertainty from the F star FSC0225−0444. The top panel shows 17 spectra of the star that have been individually calibrated from the DES photometry. As the F stars do not vary significantly, we use only the mean *gri* fluxes, measured from the 2012B semester, to compute the scale factors for each epoch. The middle spectrum shows the RMS flux computed from the 17 calibrated spectra, and the bottom spectrum shows the per cent variation. This variation spectrum demonstrates that the flux calibration is better than 5 per cent over most of the observed spectral range, and only is as poor as 10 per cent at the bluest wavelengths. This significant improvement relative to GAMA is a testament to the many improvements in the instrument, calibration procedures, and software pipeline.

3 TIME LAG MEASUREMENTS

Of the 771 AGNs OzDES is regularly monitoring, 393 of them are at the requisite redshift for the C IV line and nearby continuum to be within the wavelength range for OzDES to observe. We only consider RM using the C IV line in this paper as contamination from Fe II emission is not an issue in this wavelength range. We will present RM results for the Mg II and H β emission lines in future work. For this first study we identified a subset of these 393 AGNs that were expected to have lags of the order of 1 yr based on the $R-L$ relationship from Kaspi et al. (2007), which would be most easily observed with this partial OzDES data set. The list was further culled, primarily through visual inspection, to only include AGNs with light curves that were variable and had a high cadence. The subset consisted of 23 AGNs. For this preliminary study using the partial data set, we recovered C IV lags for two of the AGNs in this subset. The lags were measured for DES J022828.19−040044.30

[2]https://github.com/jhoormann/OzDES_calibSpec

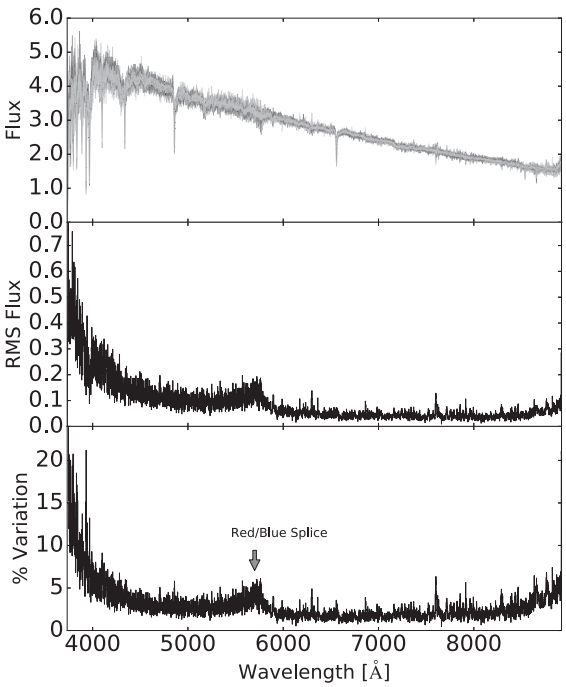

Figure 2. Seventeen spectra of the F star FSC0225−0444 taken throughout OzDES operations that we spectrophotometrically calibrated (*top panel*). In the middle panel, we show the RMS spectrum of these calibrated observations. We found the average variation (*bottom panel*) to be less than 5 per cent of the mean flux. The bump at 5700 Å is due to the dichrotic split between the red and the blue arm of the spectrograph with the noise at the far blue end being due to the reduced count rate and modest transmission losses in the flat-field lamps. All fluxes are in units of 10^{-16} erg s^{-1} cm^{-2} Å^{-1}.

at $z = 1.905$ and DES J003352.72−425452.60 at $z = 2.593$ (DES J0228−04 and DES J0033−42, respectively, in future). Fig. 3 shows the coadded spectra for the first 4 yr of OzDES for both sources. The spectrum for each individual epoch is shown in the left-hand panel of Figs 4 and 5 for DES J0228−04 and DES J0033−42. The right-hand panel isolates the continuum subtracted C IV line.

3.1 Line flux measurements

To measure line fluxes, we implemented a local continuum subtraction method to isolate the line variation from the continuum. We used two regions, located on either side of the C IV line and free of other prominent emission lines, to represent the continuum. We chose these regions, from 1450 to 1460 Å on the blue side and 1780 to 1790 Å on the red side in the rest frame, using the SDSS composite AGN spectrum (Vanden Berk et al. 2001). These regions are indicated in dark green in Fig. 3. After calculating the mean wavelength and flux in each continuum region we performed a linear fit to the data in order to model the continuum that we subtract. The local continuum model for the coadded spectra is given by the blue lines in Fig. 3.

The regions chosen to represent the continuum have the potential to significantly impact the overall line flux measurements. In order to quantify the effect the choice of continuum regions had on the resulting light curves we varied the bounds of these regions and found the resulting line flux. To do this, we first identified the regions surrounding the C IV line that could reasonably be classified as clean enough to represent the continuum, shown by the light green regions in Fig. 3. We then performed a bootstrapping procedure by randomly

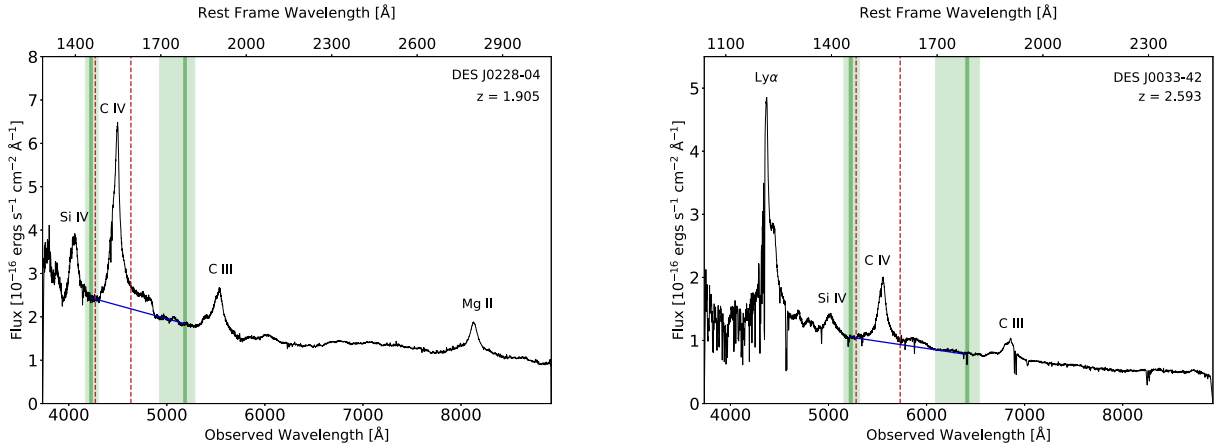

Figure 3. Coadded spectra for both AGNs studied in this paper using the first 4 yr of OzDES observations after spectrophotometric calibration. Red dashed lines indicate the integration window chosen for the C IV line. The windows used for the continuum subtraction are indicated with dark green and the local continuum model is plotted in blue. The regions used in the uncertainty calculations are shown in light green.

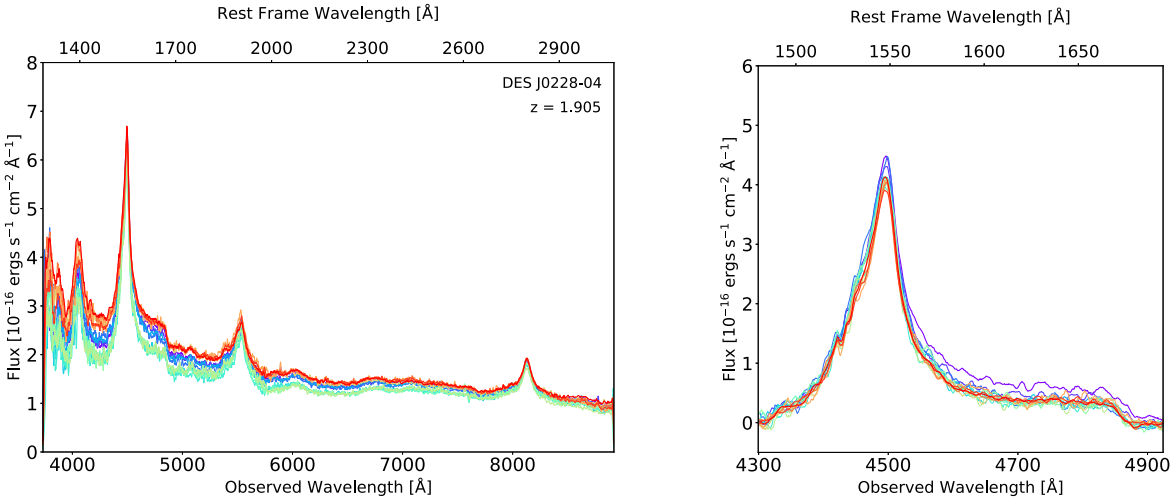

Figure 4. Smoothed spectrum for each epoch of observation of DES J0228−04. The *left-hand panel* shows the full spectrum for each epoch and the *right-hand panel* focuses in on the continuum subtracted C IV line.

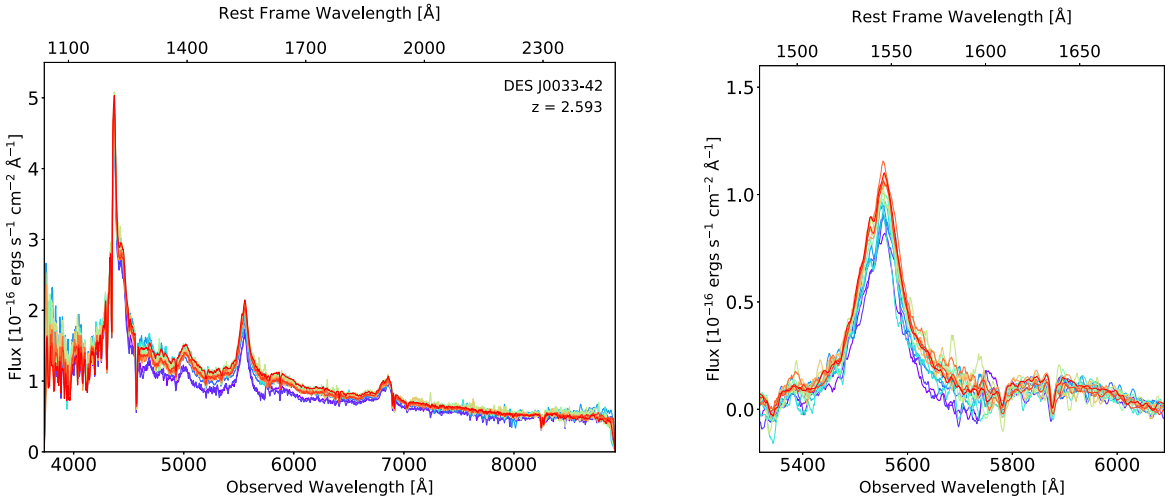

Figure 5. Smoothed spectrum for each epoch of observation of DES J0033–42. The *left-hand panel* shows the full spectrum for each epoch and the *right-hand panel* focuses in on the continuum subtracted C IV line.

Table 1. Light-curve properties for the two AGNs in this study including mean cadence and per cent error, and number of epochs during the baseline of observation.

		C IV				*g* band			
AGN	z	Epochs	Cadence (d)	Per cent error	$F_{\rm var}$	Epochs	Cadence (d)	Per cent error	$F_{\rm var}$
DES J0228−04	1.905	14	31	3.5	0.04	107	7	0.7	0.11
DES J0033−42	2.593	15	31	7.7	0.13	121	6	0.9	0.07

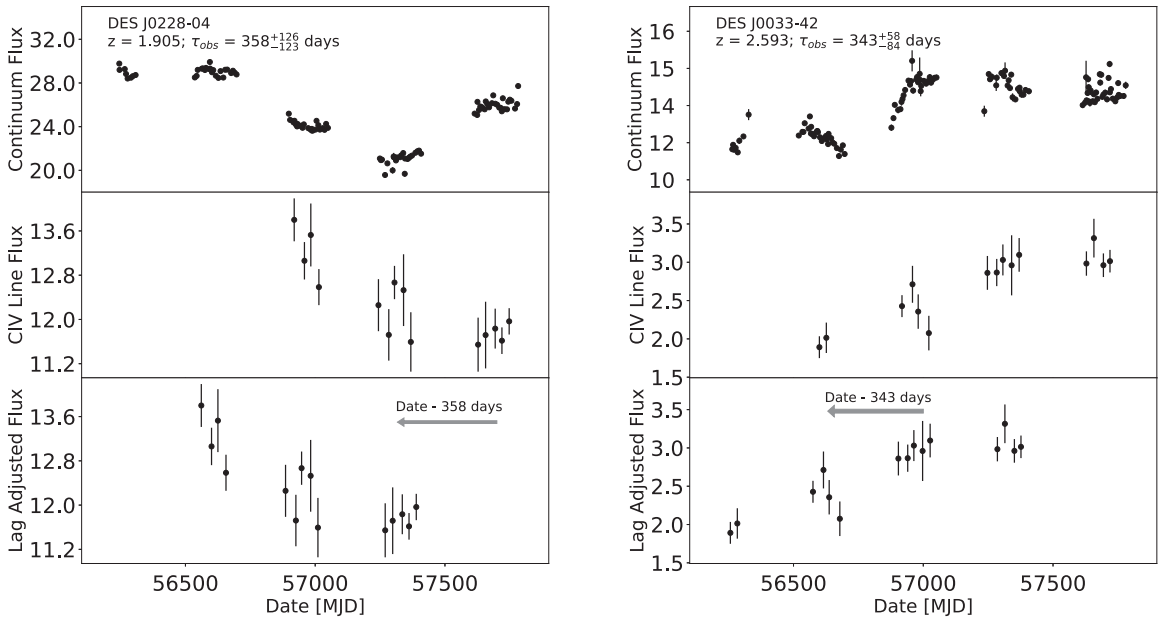

Figure 6. Light curves of the two OzDES AGNs in this study including the continuum flux represented by the DES *g*-band photometry (*top panel*) and C IV line flux measured from the OzDES spectra (*middle panel*). The C IV line light curve adjusted by the measured time lag is shown in the *bottom panel*. Fluxes are in units of 10^{-17} erg s^{-1} cm^{-2} Å^{-1}.

picking subsets of these regions to represent the continuum while resampling the fluxes from a Gaussian distribution defined by their uncertainty. The uncertainty for each flux is determined by the variance spectrum corresponding to the flux spectrum that includes both observational and calibration uncertainties for all observations in the observing run. We used the standard deviation of the distribution in the resulting line fluxes to quantify the total uncertainty included that obtained through continuum subtraction. While the regions for continuum subtraction were chosen as they are relatively clean this method does allow for any unexpected features, such as absorption lines, to be taken into account in the uncertainties. The average uncertainty in emission line flux for a given epoch was ∼3.5 per cent for DES J0228−04 and ∼7.7 per cent for DES J0033−42. Approximately 75 per cent of this uncertainty is due to the choice of region used to represent the continuum, as the slope of the continuum can significantly affect the line flux measurement. The remainder of the uncertainty is a result of the variance on the flux measurement due to observational and calibration uncertainties. The properties of these light curves including mean cadence, uncertainty, and excess variance (Rodríguez-Pascual et al. 1997) are shown in Table 1.

We calculated the mean flux density of the emission line directly from the continuum subtracted emission line spectrum over a wavelength range that was fixed throughout all observations of the source. We chose a baseline integration window for the C IV line of 1470–1595 Å. Through visual inspection we verified that this window both fully included the emission line and excluded the red shelf, a broad plateau seen near the red wing of the C IV line caused by He II λ1640 and O III λ1663 and the unidentified but prominent emission at 1600 Å (Fine et al. 2010; Assef et al. 2011). The integration window is indicated by the red dashed lines in Fig. 3.

The light curves for DES J0228−04 and for DES J0033−42 are shown in Fig. 6. The top panel shows the continuum emission, which is from the DES *g*-band photometry. The *g*-band photometry contains the 1350 Å wavelength used to represent the luminosity for high-redshift AGNs in addition to some variability due to BLR features that occur within the bandpass. This includes photometry from the first 4 yr of DES plus data from the preceding Science Verification semester (2012). The photometric light curves were constructed from the DES Year 4 catalogue, DES Y4A1, and include the DES calibration error from Burke et al. (2018). The C IV line light curves are shown in the middle panel and the C IV line light curves shifted based on the calculated time lag are shown in the bottom panel. This includes data from the first 4 yr of OzDES although DES J0228−04 had no data taken during Year 1. The C IV emission line and photometric light curves are presented in Table 2.

3.2 Lag calculations

We calculated the C IV time lags using the interpolated cross-correlation function (CCF) PYTHON code PYCCF (Sun, Grier &

Table 2. C IV and photometric light curves for the two AGNs in this study. Flux densities are in units of 10^{-17} erg s^{-1} cm^{-2} Å^{-1}. Full light curves for both AGNs are available online as machine-readable tables.

	C IV		*g* band		*r* band		*i* band	
AGN	MJD	Flux	MJD	Flux	MJD	Flux	MJD	Flux
DESJ0228−04	56919.14	13.80 ± 0.39	56245.12	29.78 ± 0.20	56245.12	16.87 ± 0.10	56253.07	14.73 ± 0.08
	56958.57	13.06 ± 0.34	56246.07	29.20 ± 0.20	56246.07	16.69 ± 0.10	56254.11	14.51 ± 0.08
	56983.13	13.53 ± 0.57	56266.16	29.27 ± 0.20	56266.17	16.87 ± 0.10	56265.16	14.28 ± 0.08
	57014.27	12.58 ± 0.33	56271.13	28.83 ± 0.20	56271.14	16.44 ± 0.09	56271.16	14.39 ± 0.08
	57243.76	12.26 ± 0.47	56277.16	28.41 ± 0.19	56277.17	16.30 ± 0.09	56277.14	14.34 ± 0.08
	57283.58	11.72 ± 0.47	56290.16	28.48 ± 0.20	56285.15	16.48 ± 0.10	56285.16	14.23 ± 0.08
	57305.58	12.67 ± 0.30	56297.10	28.62 ± 0.19	56290.17	15.89 ± 0.10	56290.19	14.27 ± 0.08
	57340.50	12.53 ± 0.65	56308.06	28.73 ± 0.20	56297.11	16.49 ± 0.09	56291.08	14.10 ± 0.07
	57368.53	11.59 ± 0.54	56536.21	28.50 ± 0.19	56306.10	16.41 ± 0.09	56297.13	14.45 ± 0.08
	57627.76	11.54 ± 0.49	56543.23	28.65 ± 0.19	56538.26	16.92 ± 0.10	56310.05	13.96 ± 0.07

Peterson 2018). This code follows the methodology of Peterson et al. (1998) that will be summarized as follows. The spectral line light curve is shifted by the time lag being tested and the continuum light curve is then interpolated to these adjusted time data points. The time-step between tested lags we use in this analysis is 3 d although tests show that the results are not sensitive to the value chosen. We cross-correlate the light curves and use the centroid of the CCF to represent the measured time lag. To determine the centroid time lag we find the peak correlation coefficient, $r_{\rm max}$, and include all values in the CCF for which $r > 0.8r_{\rm max}$. We chose the centroid lag measurement $\tau_{\rm cent}$ to represent the time lag as opposed to the peak, $\tau_{\rm peak}$, given that $\tau_{\rm cent}$ has been shown to better encapsulate the extent of the BLR (Gaskell & Sparke 1986; Robinson & Perez 1990).

In order to calculate the uncertainties on the lag measurement flux we implemented flux randomization (FR) and random subset sampling (RSS). FR accounts for the uncertainties in the flux measurements by modifying the flux used in the cross-correlation by drawing a new flux from a Gaussian distribution based on the flux and its standard deviation. To assess the impact that data sampling has on the lag measurements we also use the PYCCF code's RSS that chooses a random subset of the data (∼37 per cent smaller than the original set) on which to perform the lag calculation. In this analysis we used 10 000 realizations for the FR/RSS. We then formed a cross-correlation centroid distribution (CCCD) from the lags measured from each realization. We measure the overall time lag from the median of the CCCD and the uncertainties are the limits such that $\tau_{\rm cent} \pm \Delta\tau$ contains 68.27 per cent of the data. In order for a lag measurement to be added to the CCCD the peak of the CCF must be greater than 0.5. If the peak of the CCF lies below this value the realization is said to have failed.

3.3 OzDES lag measurements

The results of PYCCF for the two OzDES AGNs are shown in Fig. 7. The CCF is shown in the top panel and the horizontal red line shows the $0.8r_{\rm max}$ value for this CCF. The centroid of the data found above this line is used to represent the time lag, $\tau_{\rm cent}$, for this realization. The CCCD from the $\tau_{\rm cent}$ values for 10 000 realization using FR/RSS is shown in the bottom panel. Only 0.3 per cent of the realizations for DES J0228−04 failed to recover a lag resulting in an observed lag of $\tau_{\rm obs} = 358^{+126}_{-123}$ d. The analysis for DES J0033−42 only failed to recover a lag for 7 per cent the realizations with a resulting time lag of $\tau_{\rm obs} = 343^{+58}_{-84}$ d. The results of this analysis are summarized in Table 3. We ran the analysis using the *r* and *i* bands and the results are consistent within error with those obtained using the *g* band. Previous studies have reported lag measurements with failure rates of 17 per cent or even higher (Kaspi et al. 2007; Lira et al. 2018). Even if we raise the correlation coefficient threshold to 0.7, less than 10 per cent of the realizations fail for both AGNs. Our two lag measurements are consequently of higher significance than some previous measurements. The bottom panel also shows the CCCD that has been down-weighted by the overlap between the light curves considering both survey length and the seasonal gaps. This procedure will be described in detail in Section 3.4.3.

3.4 Method justification

3.4.1 Direct integration versus line fitting

We measure the line flux density by directly integrating the spectrum within the wavelength window described in Section 3.1 (red dashed lines in Fig. 3). We also experimented with parametrized fits to the emission lines. The line fitting was done after continuum subtraction and individual components of composite fits were allowed to be offset from each other in order to encapsulate any asymmetries in the wings. The effect of line fitting has on the shape of the emission line light curve is shown in Fig. 8. The black squares show the C IV light curve for each of the AGN used in this study and their corresponding uncertainties. The line flux measurements are also plotted after the emission line is fitted with different functions. The functions shown here are a Voigt profile (blue circles), a double Gaussian (red triangle), and a triple Gaussian (green diamond). The line fluxes calculated with these different fits lie within the error bars of the line flux calculated by directly integrating the emission line. Furthermore, the resulting lag measurements using these fits differ by only a few days, well within the uncertainties of the lag measurements. This indicates that the parametrized fits to the emission line do not provide any significant benefit.

3.4.2 Line integration window

It is also important to determine the significance of the choice of line integration window on the lag measurement, particularly given the presence of the red shelf so close to the C IV line. We quantified this by randomly selecting an integration window with a left bound in the range of 1456–1506 Å and a right bound in the range of 1570–1634 Å. This tests the effects of introducing more continuum emission, including the red shelf, and also cutting off the wings

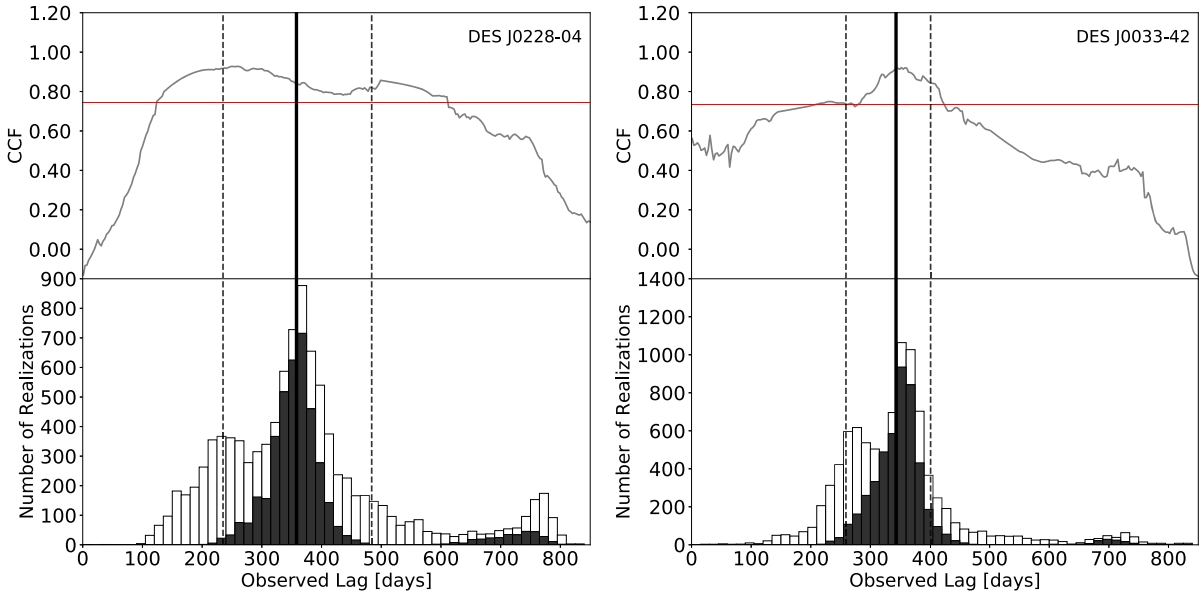

Figure 7. Lag calculations of the two OzDES AGNs. The CCF for each AGN are shown in the *top panel*. The centroid of the CCF above the red line at $0.8r_{\rm max}$ is used to determine the time lag for each realization. The final time lag is the median of the CCCD (*bottom panel*) that is determined using FR/RSS on the light curves with 10 000 realizations. The solid black line represents the measured time lag and the dotted lines mark the 68 per cent confidence levels. The dark grey histogram is the CCCD if we down-weight lags that correspond to light curves with minimal overlap due to the seasonal gaps. The time lags we report are based on the original CCCD (white).

Table 3. Parameters of the two AGNs in this study.

AGN	z	$\tau_{\rm obs}$ (d)	$\tau_{\rm RF}$ (d)	$\log \lambda L_{\lambda}$ (erg s^{-1})	$\sigma_{\rm RMS}$ (km s^{-1})	$M_{\rm BH}$ (10^9 M$_{\odot}$)	$M_{\rm VP}$ (10^9 M$_{\odot}$)
DES J0228–04	1.905	358^{+126}_{-123}	123^{+43}_{-42}	46.43 ± 0.04	6365 ± 66	$4.4^{+2.0}_{-1.9}$	$1.0^{+0.3}_{-0.3}$
DES J0033–42	2.593	343^{+58}_{-84}	95^{+16}_{-23}	46.51 ± 0.02	6250 ± 64	$3.3^{+1.1}_{-1.2}$	$0.7^{+0.1}_{-0.2}$

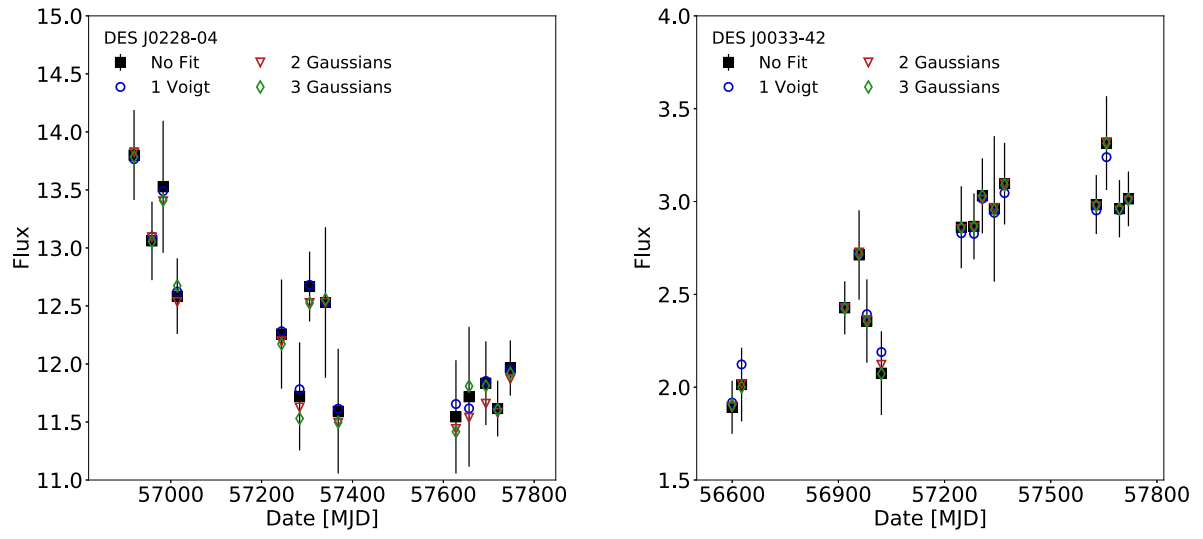

Figure 8. Results from the test to determine the validity of directly integrating the calibrated spectra. Light curves measured from direct integration are shown by black squares with error bars. Line fluxes calculated after fitting the spectra with various line profiles lie within these uncertainties (Voigt profile – blue circle, double Gaussian – red triangle, triple Gaussian – green diamond). Fluxes are in units of 10^{-17} erg s^{-1} cm^{-2} Å^{-1}.

of the emission line in order to avoid features not part of the C IV line. After randomly choosing 500 new integration windows we remade the light curves that we then used to measure the time lag, $\tau_{\rm cent}$. The results of this study can be seen in Fig. 9. While there is some distribution in the recovered lag values, the result is always smaller than the uncertainties in the lag measurement. We therefore conclude that the choice of integration window does not significantly affect our results. As mentioned previously the

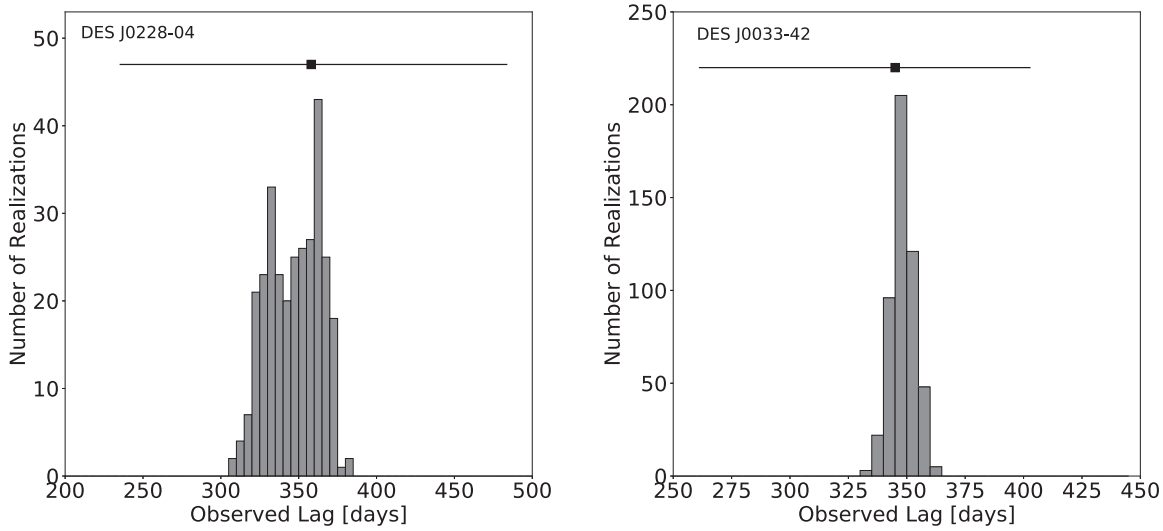

Figure 9. Results from test to determine the significance of the choice of integration window. Distributions of the lags, $\tau_{\rm cent}$, resulting from a sampling of 500 random integration windows. The data point shows the lag value and corresponding uncertainty using the integration window used in this paper (1470–1595 Å). The distribution of lags resulting from the various integration windows falls within the uncertainty associated with the lag measurement.

OzDES spectra are made by splicing the red and blue arm of the spectrograph around ∼5700 Å. During Year 1 some of the spectra show a discontinuity where the splice occurs. OzDES procedures were modified from Year 2 onward to mitigate the effect. For DES J0033−42 this splice occurs at the rest-frame wavelength of 1586 Å that is within the integration window. However, the results shown in Fig. 9 indicate that this splicing does not significantly bias our results as the randomly selected integration windows include ones that fully exclude the splice.

3.4.3 Time lag prior

One assumption that can have a significant effect on the measured lag as well as the uncertainties is the prior placed on the time lag. This study assumes the time lag will fall between 0 and 850 d. We have tested this assumption in three ways.

Test 1: We begin by determining the CCCD without any lag prior. This is shown by the white histogram in the top panel of Fig. 10. The corresponding time lag measurements are shown by the grey data point above the CCCD. However, if we put a prior on the time lag, i.e. that the lag should be positive, the resulting time lag and uncertainties can be significantly affected. For example, for both AGNs the prior enforcing the assumption of a positive lag is shown in red. The upper limit for each AGN (850 d for DES J0228−04 and 1119 d for DES J0033−42) is determined by the baseline of the observations. If the C IV line light curve is shifted by a lag value greater than this there will be no overlap between the continuum and line light curves meaning any lag measurements are primarily dependent on extrapolation, not measured data, and are therefore unreliable. We also tested smaller lag prior ranges.

For all the lag ranges shown, over 50 per cent of the original CCCD falls within these values. This indicates that a significant amount of data is not excluded by the choice of lag prior and any resulting lag measurements are reasonable (see e.g. Lira et al. 2018). For DES J0228−04 over 70 per cent of the original CCCD falls within the smallest lag range (0–600 d) while for DES J0033−42 65 per cent falls within this range.

Test 2: We performed a second test to motivate our lag prior choice using a weighting scheme derived by Grier et al. (2017b) to down-weight lags that occur where there is little overlap between the two light curves after adjusting for the time lag. Following this prescription each lag in the CCCD is weighted by the function $w = (N_{\rm lag}/N_0)^2$. The number of overlapping data points with no lag correction is given by N_0 and the number of overlapping data points after lag correction is $N_{\rm lag}$. Lags with a low number of overlapping data points rely heavily on the extrapolation assumed, not the real measured data points. This makes these lag values less reliable. The bottom panel of Fig. 10 shows the original CCCD in white with the CCCD down-weighted using this prescription to account for the length of the survey shown by the light grey region. This eliminates much of the data at negative lags and the slight bump after 1000 d seen for DES J0033−42.

Test 3: This original weighting scheme only takes into account the baseline of the OzDES observations as this is most directly related to the prior we can place on the lag measurements. However, an important feature of the OzDES survey is the seasonal gaps of around 200 d between each observing season. In order to test the significance the seasonal gaps have on our ability to recover time lags we modified the weighting procedure to account for the case when there is no overlap between the light curves because the lag moves the line light curve into the seasonal gaps of the continuum light curves. This is shown by the dark grey histogram that significantly decreases the width of the main peak.

As a result of this analysis we choose to report our results using the lag prior of 0–850 d. This is shown by the white histogram on the lower panel of Fig. 7. On Fig. 7, we also plot the CCCD after down-weighting lags based on survey length and seasonal gaps (dark grey histogram). We use the unweighted CCCD for our final result in order to avoid biasing the analysis by only considering lags to which the survey is sensitive. However, the down-weighted CCCD does shed light into the importance of the cadence of the observations. Specifically, the peaks in the CCCD around 200 d are likely due to the seasonal gaps in OzDES which shows that survey cadence is an important limiting factor and source of uncertainty in lag recovery.

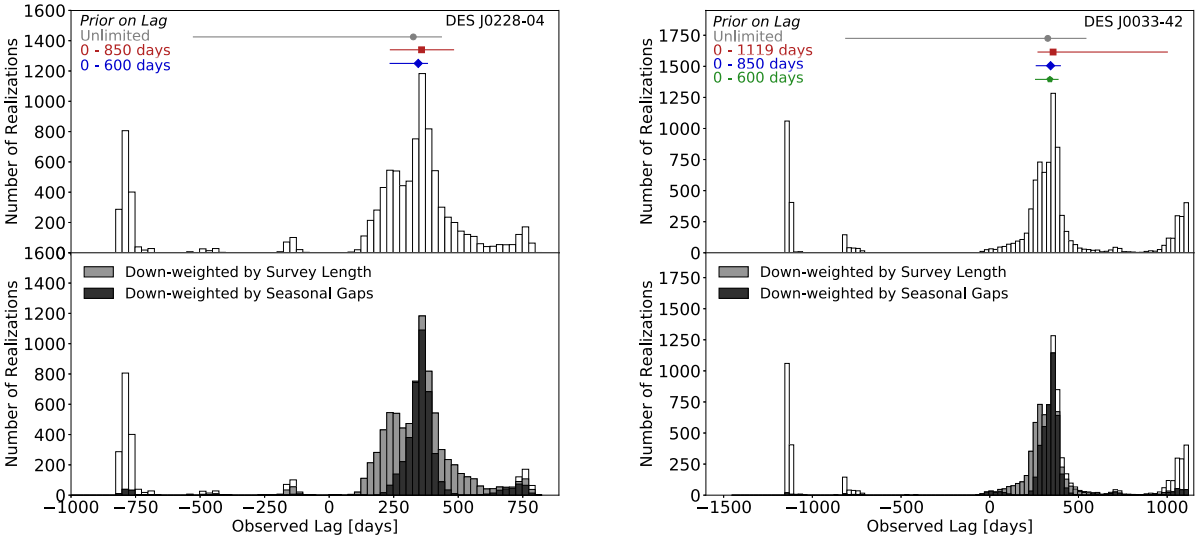

Figure 10. Results from the test to determine the effect of the time lag prior on the measured lag. The *top panel* shows the effect of the prior on the lag measurement. The white histogram shows the CCCD with no prior placed on the time lag. The lag measurements and uncertainties are shown for different lag priors by the data points above the CCCD. The *bottom panels* show which portions of the CCCD are affected when down-weighting for survey length (light grey) and including the seasonal gaps (dark grey).

4 RESULTS

4.1 Black hole mass

We need to know the velocity distribution of the BLR clouds in order to determine the black hole mass. The velocity can be measured from either the mean spectrum or the root mean squared (RMS) spectrum, which isolates the reverberating components of the emission line. A smoothed version of both the mean and RMS spectrum for each AGN is shown in Fig. 11. The velocity can be characterized by either the velocity dispersion (σ) or the full width at half-maximum (FWHM). Fig. 11 includes the FWHM and σ values for each spectrum calculated within the line integration window indicated by the vertical red lines. The line widths have been corrected for the resolution of the spectrograph that is ∼3 Å. For our black hole mass calculations we used the line dispersion, σ, of the RMS spectrum to measure the velocity of the BLR clouds, as work by Peterson et al. (2004) concluded that the line dispersion is the best representation of the BLR velocity. We calculated the uncertainties by performing a bootstrapping procedure similar to that described above to account for the impact of continuum subtraction and uncertainties on the flux values before calculating the line width. Note that the RMS spectrum for DES J0033−42 (bottom right panel) has a distinct plateau on the red side of the line. This is due to the splicing between the red and blue arms of the spectrograph at ∼5700 Å. The plateau is less pronounced if the spectra from Year 1 are not included in the calculation of the RMS spectrum. Regardless of whether or not the Year 1 data is included the measurement of the velocity dispersion does not change significantly. This is shown by the blue line in the right-hand panel of Fig. 11. There is still some increase in flux around the splice. If the right edge of the integration window within which the line width is calculated is shifted to completely exclude the splice (1580 Å in the rest frame) the line width decreases by around 650 km s^{-1} for both AGNs and the resulting black hole mass is consistent with those obtained when considering the full integration window. This indicates that the effect of the red/blue arm splice is a subdominant effect here but a more rigorous analysis of the line width measurements will be done in the future.

The black hole masses are $4.4^{+2.0}_{-1.9} \times 10^9$ M$_\odot$ for DES J0228−04 and $3.3^{+1.1}_{-1.2} \times 10^9$ M$_\odot$ for DES J0033−42 (see Table 3). We calculated the masses using equation (1) and $f = 4.47 \pm 1.25$ (Woo et al. 2015).

4.2 Radius–luminosity relationship

Previous radius–luminosity relationships using the C IV line measurements were made using the λL_λ(1350 Å) luminosity (Peterson et al. 2005; Kaspi et al. 2007; Trevese et al. 2014; Lira et al. 2018). They were generally found using the Bivariate Correlated Errors and Intrinsic Scatter (BCES) method developed by Akritas & Bershady (1996) to account for uncertainties in both luminosity and radius. For low-luminosity AGNs, Peterson et al. (2005) found a slope of 0.61 ± 0.05. Including higher luminosity measurements Kaspi et al. (2007) found a slope of 0.55 ± 0.04 and 0.52 ± 0.04 using the FITEXY method to iteratively minimize χ^2 (Press et al. 1992) combined with the intrinsic scatter prescription of Tremaine et al. (2002). Most recently Lira et al. (2018) published a $R-L$ slope of 0.46 ± 0.08. We have constructed a new $R-L$ relationship by adding our two OzDES lag measurements to those in Kaspi et al. (2007), Trevese et al. (2014), and the four most robust C IV lag measurements (CT286, CT406, J214355, J221516) made by Lira et al. (2018). Those four were measured at a 1σ level with a < 60 per cent failure rate. The results we used from the literature are summarized in Table 4. We calculated the λL_λ(1350 Å) luminosity for the OzDES AGNs assuming $H_0 = 70$ km s^{-1} Mpc^{-1}, $\Omega_M = 0.3$, and $\Omega_\Lambda = 0.7$. The resulting $R-L$ diagram can be seen in Fig. 12. We find that the best-fitting slope is 0.49 ± 0.02 for the following R–L relationship:

$$\log R(\mathrm{lt-days}) = (0.82 \pm 0.08) + (0.49 \pm 0.02) \log \left(\frac{\lambda L_\lambda (1350\ \text{Å})}{10^{44}\ \mathrm{erg\ s^{-1}}} \right), \quad (2)$$

based on the public BCES code by Nemmen et al. (2012). As the BCES method does not account for asymmetry in the error bars we calculated the slope using both the upper and lower values for uncertainties in the radius. This did not affect the resulting slope, intercept, or corresponding uncertainties. Our

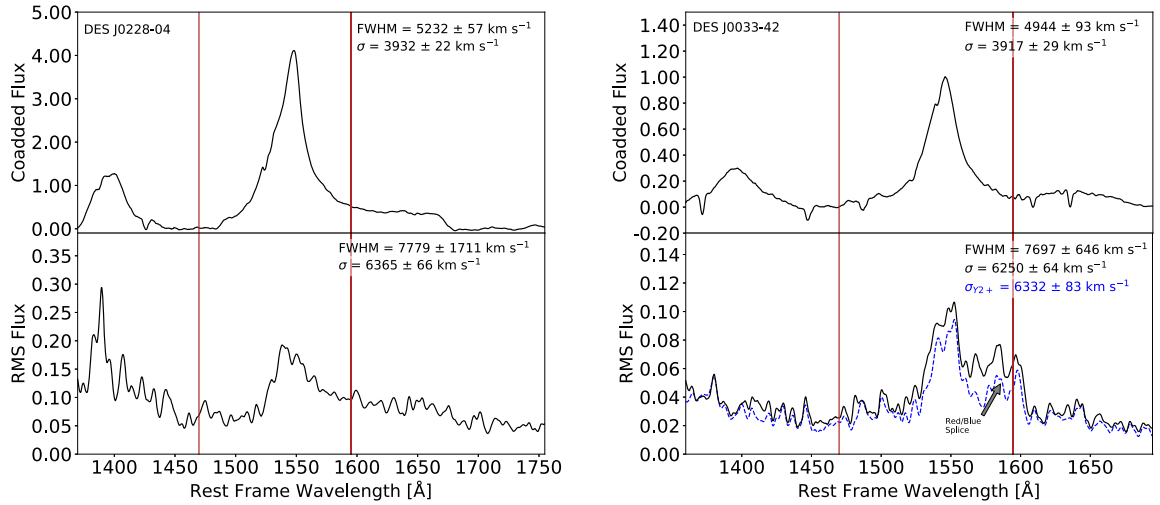

Figure 11. Smoothed coadded spectrum (*top panel*) and smoothed RMS spectrum (*bottom panel*) for each of the AGN used to calculate both the FWHM and velocity dispersion. The line integration window is indicated by the red lines. All fluxes are in units of 10^{-16} erg s^{-1} cm^{-2} Å^{-1}. The plateau on the red side of the line for DES J0033−42 is due to the splicing of the red/blue arms of the spectrograph at 5700 Å in the observed frame that is more pronounced during the first 2 yr of observation. The blue line shows the RMS spectrum with the first year removed with a corresponding velocity dispersion of $\sigma_{Y2+} = 6332 \pm 83$ km s^{-1}.

Table 4. Rest-frame time lags and 1350 Å luminosities for all C IV lags used to derive the $R-L$ relationship.

AGN	$\log \lambda L_\lambda$ (erg s^{-1})	τ_{RF} (d)	Ref.
DES J0228−04	46.43 ± 0.04	123^{+43}_{-42}	1
DES J0033−42	46.51 ± 0.02	95^{+16}_{-23}	1
NGC 4395 Visit 2	39.57 ± 0.06	$0.033^{+0.017}_{-0.013}$	2
NGC 4395 Visit 3	40.10 ± 0.03	$0.046^{+0.017}_{-0.013}$	2
NGC 3783	43.59 ± 0.09	$4.0^{+1.0}_{-1.5}$	2
NGC 5548 Year 1	43.66 ± 0.14	$9.8^{+1.9}_{-1.5}$	2
NGC 5548 Year 5	43.58 ± 0.06	$6.7^{+0.9}_{-1.0}$	2
NGC 7469	43.78 ± 0.07	$2.5^{+0.3}_{-0.2}$	2
3C 390.3	44.07 ± 0.21	$35.7^{+11.4}_{-14.6}$	2
S5 0836+71	47.05 ± 0.06	188^{+27}_{-37}	3
PG 1247+267	47.47 ± 0.003	142^{+26}_{-25}	4
CT286	47.05 ± 0.12	459^{+71}_{-92}	5
CT406	46.91 ± 0.05	115^{+64}_{-86}	5
J214355	46.96 ± 0.07	128^{+91}_{-82}	5
J221516	47.16 ± 0.12	165^{+98}_{-13}	5

Note. References: (1) This work; (2) Peterson et al. (2005), and references therein; (3) Kaspi et al. (2007); (4) Trevese et al. (2014); (5) Lira et al. (2018).

results are also consistent with a Monte Carlo linear regression procedure that varies the data points within their asymmetrical error bars. While yielding the same slope the $R-L$ relationship using the existing data summarized in Table 3 but without including the two OzDES AGNs has a larger error of 0.03.

When comparing our measured time lags with those estimated from previous $R-L$ relationships the lags measured by Kaspi et al. (2007) are 50 per cent and 110 per cent larger for DES J0228−04 and DES J0033−42, respectively. The slope derived in Kaspi et al. (2007) is consistent with the high-redshift relationship $R(\mathrm{H}\,\beta) \propto \lambda L_\lambda(1350\ \text{Å})^{0.56}$ (Kaspi et al. 2005). However, this slope was using a data set that only included one high-luminosity measurement. Our lags are consistent within the measured error bars with the lags predicted by the most recent $R-L$ relationship found by Lira et al. (2018) that included the higher luminosity AGNs. Using the dispersion-based single epoch mass estimate for C IV found by Vestergaard & Peterson (2006), the black hole masses are 4.2×10^9 M$_\odot$ for DES J0228−04 and 4.5×10^9 M$_\odot$ for DES J0033−42 that are comparable with the masses derived in this paper.

5 CONCLUSION

In this paper, we present the first OzDES RM black hole mass measurements using the C IV line for some of the highest quality AGNs observed during the first 4 yr of OzDES operations. The techniques tested and implemented here will now be used on the wider OzDES sample and will include an additional 2 yr baseline once the data from Year 5 and 6 have been processed. The data obtained from OzDES is complementary to its Northern hemisphere counterpart, the Sloan Digital Sky Survey Reverberation Mapping program (SDSS-RM) (Shen et al. 2015). Similar to OzDES, SDSS-RM observed 849 AGNs out to $z < 4.5$. The primary difference between them is that SDSS-RM has published results based on approximately 30 epochs of observations over 6 months whereas OzDES has around 23 epochs over 6 yr.

We measured black hole masses of 4.4×10^9 M$_\odot$ for DES J0228−04 and 3.3×10^9 M$_\odot$ for DES J0033−42. These are amongst the highest redshift AGNs with the highest mass black holes measured to date with this technique. We have used these new measurements to update the C IV $R-L$ relationship and derive the slope of $\alpha = 0.49 \pm 0.02$. Of the 771 AGNs regularly observed with OzDES, those with C IV lines range in luminosity from $10^{44.3}$ erg s$^{-1} \leq \lambda L_\lambda(1350\ \text{Å}) \leq 10^{47.2}$ erg s^{-1}. Based on this range in luminosities we expect to be able to fill in the gap between moderate luminosity AGNs ($\sim 10^{43}$ erg s^{-1}) and high-luminosity AGNs ($> 10^{46}$ erg s^{-1}) that is seen in Fig. 12. This will provide an opportunity to investigate the source of the scatter seen in this relationship.

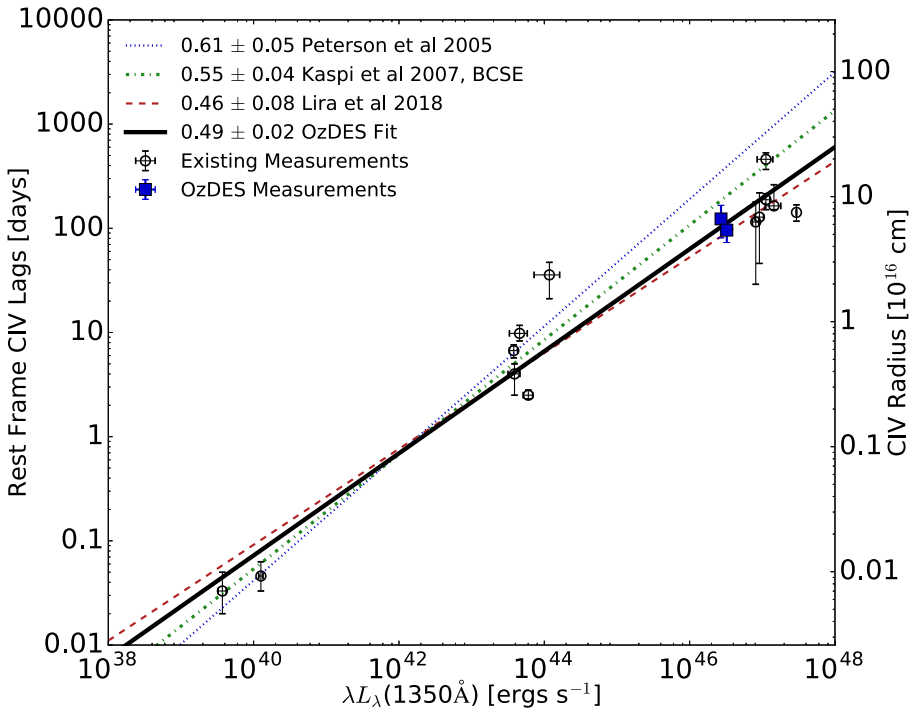

Figure 12. Rest-frame C IV lag versus the AGN luminosity λL_λ(1350 Å). Previous lag measurements (Peterson et al. 2005; Kaspi et al. 2007; Trevese et al. 2014; Lira et al. 2018) are indicated with black circles and the OzDES measurements are shown in blue squares. Table 4 summarizes the data used in this figure. The best-fitting line to the entire data set is the black line with a slope of 0.49 ± 0.02 found using the BCES method. Best-fitting lines obtained by Peterson et al. (2005) (blue dotted line) including the low-luminosity sources and the Kaspi et al. (2007) BCES result (green dashed dotted) that extended the fit to higher luminosities are shown for comparison. The red dashed line corresponds to that measured by Lira et al. (2018). The corresponding C IV BLR radius in cm is also shown.

In order to study the stratification of the BLR we chose the OzDES AGN candidates to include AGNs where multiple emission lines that are in the observed spectroscopic bandpass. Our data set includes 148 AGNs, such as DES J0228−04, which contain both C IV and Mg II and 27 AGNs which include Mg II and H β. Given the high-redshift range of the OzDES RM candidates, $0.1 < z < 4.5$, we will have the opportunity to study the growth of supermassive black holes and test the theory that AGNs can be used as high-redshift standard candles.

ACKNOWLEDGEMENTS

This research was funded partially by the Australian Government through the Australian Research Council through project DP160100930. PM and ZY were supported in part by the United States National Science Foundation under grant no. 161553.

Based on data acquired at the Anglo-Australian Telescope, under program A/2013B/012. We acknowledge the traditional owners of the land on which the AAT stands, the Gamilaraay people, and pay our respects to elders past and present.

Funding for the DES Projects has been provided by the U.S. Department of Energy, the U.S. National Science Foundation, the Ministry of Science and Education of Spain, the Science and Technology Facilities Council of the United Kingdom, the Higher Education Funding Council for England, the National Center for Supercomputing Applications at the University of Illinois at Urbana-Champaign, the Kavli Institute of Cosmological Physics at the University of Chicago, the Center for Cosmology and Astro-Particle Physics at the Ohio State University, the Mitchell Institute for Fundamental Physics and Astronomy at Texas A&M University, Financiadora de Estudos e Projetos, Fundação Carlos Chagas Filho de Amparo à Pesquisa do Estado do Rio de Janeiro, Conselho Nacional de Desenvolvimento Científico e Tecnológico and the Ministério da Ciência, Tecnologia e Inovação, the Deutsche Forschungsgemeinschaft, and the Collaborating Institutions in the Dark Energy Survey.

The Collaborating Institutions are Argonne National Laboratory, the University of California at Santa Cruz, the University of Cambridge, Centro de Investigaciones Energéticas, Medioambientales y Tecnológicas-Madrid, the University of Chicago, University College London, the DES-Brazil Consortium, the University of Edinburgh, the Eidgenössische Technische Hochschule (ETH) Zürich, Fermi National Accelerator Laboratory, the University of Illinois at Urbana-Champaign, the Institut de Ciències de l'Espai (IEEC/CSIC), the Institut de Física d'Altes Energies, Lawrence Berkeley National Laboratory, the Ludwig-Maximilians Universität München and the associated Excellence Cluster Universe, the University of Michigan, the National Optical Astronomy Observatory, the University of Nottingham, The Ohio State University, the University of Pennsylvania, the University of Portsmouth, SLAC National Accelerator Laboratory, Stanford University, the University of Sussex, Texas A&M University, and the OzDES Membership Consortium.

Based in part on observations at Cerro Tololo Inter-American Observatory, National Optical Astronomy Observatory, which is operated by the Association of Universities for Research in Astronomy (AURA) under a cooperative agreement with the National Science Foundation.

The DES data management system is supported by the National Science Foundation under grant numbers AST-1138766 and AST-1536171. The DES participants from Spanish institutions are partially supported by MINECO under grants AYA2015-71825, ESP2015-66861, FPA2015-68048, SEV-2016-0588, SEV-2016-0597, and MDM-2015-0509, some of which include ERDF funds from the European Union. IFAE is partially funded by the CERCA program of the Generalitat de Catalunya. Research leading to these results has received funding from the European Research Council under the European Union's Seventh Framework Program (FP7/2007-2013) including ERC grant agreements 240672, 291329, and 306478. We acknowledge support from the Australian Research Council Centre of Excellence for All-sky Astrophysics (CAASTRO), through project number CE110001020, and the Brazilian Instituto Nacional de Ciência e Tecnologia (INCT) e-Universe (CNPq grant 465376/2014-2).

This manuscript has been authored by Fermi Research Alliance, LLC under Contract No. DE-AC02-07CH11359 with the U.S. Department of Energy, Office of Science, Office of High Energy Physics. The United States Government retains and the publisher, by accepting the article for publication, acknowledges that the United States Government retains a non-exclusive, paid-up, irrevocable, world-wide license to publish or reproduce the published form of this manuscript, or allow others to do so, for United States Government purposes.

REFERENCES

Abbott T. M. C. et al., 2018, MNRAS, 480, 3879
Akritas M. G., Bershady M. A., 1996, ApJ, 470, 706
Assef R. J. et al., 2011, ApJ, 742, 93
Bentz M. C., Peterson B. M., Netzer H., Pogge R. W., Vestergaard M., 2009, ApJ, 697, 160
Bentz M. C. et al., 2013, ApJ, 767, 149
Blandford R. D., McKee C. F., 1982, ApJ, 255, 419
Burke D. L. et al., 2018, AJ, 155, 41
Chang C. et al., 2018, MNRAS, 475, 3165
Childress M. J. et al., 2017, MNRAS, 472, 273
Clavel J. et al., 1991, ApJ, 366, 64
D'Andrea C. B. et al., 2018, AJ, preprint(arXiv:1811.09565)
Dark Energy Survey Collaboration, 2016, MNRAS, 460, 1270
Davies R. I. et al., 2006, ApJ, 646, 754
Denney K. D. et al., 2010, ApJ, 721, 715
Diehl H. T. et al., 2016, in Proc. SPIE Conf. Ser. Vol. 9910, Observatory Operations: Strategies, Processes, and Systems VI. SPIE, Bellingham, p. 99101D
Diehl H. T. et al., 2018, in Proc. SPIE Conf. Ser. Vol. 1070, Observatory Operations: Strategies, Processes, and Systems VII. SPIE, Bellingham, p. 107040D
Elvin-Poole J. et al., 2018, Phys. Rev. D, 98, 042006
Ferrarese L., Ford H., 2005, Space Sci. Rev., 116, 523
Ferrarese L., Merritt D., 2000, ApJ, 539, L9
Fine S., Croom S. M., Bland-Hawthorn J., Pimbblet K. A., Ross N. P., Schneider D. P., Shanks T., 2010, MNRAS, 409, 591
Flaugher B., 2005, Int. J. Mod. Phys. A, 20, 3121
Flaugher B. et al., 2015, AJ, 150, 150
Gaskell C. M., Sparke L. S., 1986, ApJ, 305, 175
Gebhardt K. et al., 2000a, ApJ, 539, L13
Gebhardt K. et al., 2000b, ApJ, 543, L5
Grier C. J. et al., 2012, ApJ, 755, 60
Grier C. J. et al., 2013, ApJ, 773, 90
Grier C. J., Pancoast A., Barth A. J., Fausnaugh M. M., Brewer B. J., Treu T., Peterson B. M., 2017a, ApJ, 849, 146
Grier C. J. et al., 2017b, ApJ, 851, 21
Hicks E. K. S., Malkan M. A., 2008, ApJS, 174, 31
Hopkins A. M. et al., 2013, MNRAS, 430, 2047
Kaspi S., Smith P. S., Netzer H., Maoz D., Jannuzi B. T., Giveon U., 2000, ApJ, 533, 631
Kaspi S., Maoz D., Netzer H., Peterson B. M., Vestergaard M., Jannuzi B. T., 2005, ApJ, 629, 61
Kaspi S., Brandt W. N., Maoz D., Netzer H., Schneider D. P., Shemmer O., 2007, ApJ, 659, 997
Kessler R. et al., 2015, AJ, 150, 172
King A. L., Davis T. M., Denney K. D., Vestergaard M., Watson D., 2014, MNRAS, 441, 3454
King A. L. et al., 2015, MNRAS, 453, 1701
Kormendy J., Ho L. C., 2013, ARA&A, 51, 511
Kormendy J., Richstone D., 1995, ARA&A, 33, 581
Lewis I. J. et al., 2002, MNRAS, 333, 279
Lira P. et al., 2018, ApJ, 865, 56
McConnell N. J., Ma C.-P., 2013, ApJ, 764, 184
McLure R. J., Jarvis M. J., 2002, MNRAS, 337, 109
Metzroth K. G., Onken C. A., Peterson B. M., 2006, ApJ, 647, 901
Morganson E. et al., 2018, PASP, 130, 074501
Mudd D. et al., 2018, ApJ, 862, 123
Nemmen R. S., Georganopoulos M., Guiriec S., Meyer E. T., Gehrels N., Sambruna R. M., 2012, Science, 338, 1445
Onken C. A. et al., 2014, ApJ, 791, 37
Pancoast A., Brewer B. J., Treu T., 2014, MNRAS, 445, 3055
Peterson B. M., 1993, PASP, 105, 247
Peterson B. M., Horne K., 2004, Astron. Nachr., 325, 248
Peterson B. M., Wanders I., Horne K., Collier S., Alexander T., Kaspi S., Maoz D., 1998, PASP, 110, 660
Peterson B. M. et al., 2004, ApJ, 613, 682
Peterson B. M. et al., 2005, ApJ, 632, 799
Press W. H., Teukolsky S. A., Vetterling W. T., Flannery B. P., 1992, Numerical Recipes in FORTRAN. The Art of Scientific Computing, 2nd ed. Cambridge Univ. Press, Cambridge
Reichert G. A. et al., 1994, ApJ, 425, 582
Richstone D. et al., 1998, Nature, 395, A14
Robinson A., Perez E., 1990, MNRAS, 244, 138
Rodríguez-Pascual P. M. et al., 1997, ApJS, 110, 9
Shen Y. et al., 2015, ApJS, 216, 4
Shen Y. et al., 2016, ApJ, 818, 30
Smith G. A. et al., 2004, in Moorwood A. F. M., Iye M., eds, Proc. SPIE Conf. Ser. Vol. 5492, Ground-based Instrumentation for Astronomy. SPIE, Bellingham, p. 410
Sun M., Grier C. J., Peterson B. M., 2018, Astrophysics Source Code Library, record ascl:1805.032
Tie S. S. et al., 2017, AJ, 153, 107
Trakhtenbrot B., Netzer H., 2012, MNRAS, 427, 3081
Tremaine S. et al., 2002, ApJ, 574, 740
Trevese D., Perna M., Vagnetti F., Saturni F. G., Dadina M., 2014, ApJ, 795, 164
Vanden Berk D. E. et al., 2001, AJ, 122, 549
Vestergaard M., 2002, ApJ, 571, 733
Vestergaard M., Peterson B. M., 2006, ApJ, 641, 689
Wandel A., Peterson B. M., Malkan M. A., 1999, ApJ, 526, 579
Wang J.-G. et al., 2009, ApJ, 707, 1334
Watson D., Denney K. D., Vestergaard M., Davis T. M., 2011, ApJ, 740, L49
Williams P. R. et al., 2018, ApJ, 866, 75
Woo J.-H. et al., 2010, ApJ, 716, 269
Woo J.-H., Yoon Y., Park S., Park D., Kim S. C., 2015, ApJ, 801, 38
Yuan F. et al., 2015, MNRAS, 452, 3047

SUPPORTING INFORMATION

Supplementary data are available at *MNRAS* online.
Table 2. C IV and photometric light curves for the two AGNs in this study.

[1]*School of Mathematics and Physics, University of Queensland, Brisbane, QLD 4072, Australia*
[2]*Center for Cosmology and Astro-Particle Physics, The Ohio State University, Columbus, OH 43210, USA*
[3]*Department of Astronomy, The Ohio State University, Columbus, OH 43210, USA*
[4]*School of Physics, University of Melbourne, Parkville, VIC 3010, Australia*
[5]*The Research School of Astronomy and Astrophysics, Australian National University, ACT 2601, Australia*
[6]*Department of Physics and Astronomy, University of California, Irvine, Irvine, CA 92697, USA*
[7]*Fermi National Accelerator Laboratory, PO Box 500, Batavia, IL 60510, USA*
[8]*Korea Astronomy and Space Science Institute, Yuseong-gu, Daejeon 305-348, South Korea*
[9]*Institute of Cosmology and Gravitation, University of Portsmouth, Portsmouth PO1 3FX, UK*
[10]*Institute of Astronomy, University of Cambridge, Madingley Road, Cambridge CB3 0HA, UK*
[11]*Kavli Institute for Cosmology, University of Cambridge, Madingley Road, Cambridge CB3 0HA, UK*
[12]*Department of Physics & Astronomy, University College London, Gower Street, London WC1E 6BT, UK*
[13]*Kavli Institute for Particle Astrophysics & Cosmology, PO Box 2450, Stanford University, Stanford, CA 94305, USA*
[14]*SLAC National Accelerator Laboratory, Menlo Park, CA 94025, USA*
[15]*Centro de Investigaciones Energéticas, Medioambientales y Tecnológicas (CIEMAT), Madrid, Spain*
[16]*Laboratório Interinstitucional de e-Astronomia – LIneA, Rua Gal. José Cristino 77, Rio de Janeiro, RJ 20921-400, Brazil*
[17]*INAF, Astrophysical Observatory of Turin, I-10025 Pino Torinese, Italy*
[18]*Department of Astronomy, University of Illinois at Urbana-Champaign, 1002 W. Green Street, Urbana, IL 61801, USA*
[19]*National Center for Supercomputing Applications, 1205 West Clark St., Urbana, IL 61801, USA*
[20]*Institut de Física d'Altes Energies (IFAE), The Barcelona Institute of Science and Technology, Campus UAB, E-08193 Bellaterra (Barcelona), Spain*
[21]*Institut d'Estudis Espacials de Catalunya (IEEC), E-08034 Barcelona, Spain*
[22]*Institute of Space Sciences (ICE, CSIC), Campus UAB, Carrer de Can Magrans, s/n, E-08193 Barcelona, Spain*
[23]*School of Physics and Astronomy, University of Southampton, Southampton SO17 1BJ, UK*
[24]*Department of Physics, IIT Hyderabad, Kandi, Telangana 502285, India*
[25]*Kavli Institute for Cosmological Physics, University of Chicago, Chicago, IL 60637, USA*
[26]*Instituto de Fisica Teorica UAM/CSIC, Universidad Autonoma de Madrid, E-28049 Madrid, Spain*
[27]*Department of Astronomy, University of Michigan, Ann Arbor, MI 48109, USA*
[28]*Department of Physics, University of Michigan, Ann Arbor, MI 48109, USA*
[29]*Department of Physics, Stanford University, 382 Via Pueblo Mall, Stanford, CA 94305, USA*
[30]*Department of Physics, ETH Zurich, Wolfgang-Pauli-Strasse 16, CH-8093 Zurich, Switzerland*
[31]*Santa Cruz Institute for Particle Physics, Santa Cruz, CA 95064, USA*
[32]*Department of Physics, The Ohio State University, Columbus, OH 43210, USA*
[33]*Max Planck Institute for Extraterrestrial Physics, Giessenbachstrasse, D-85748 Garching, Germany*
[34]*Universitäts-Sternwarte, Fakultät für Physik, Ludwig-Maximilians Universität München, Scheinerstr 1, D-81679 München, Germany*
[35]*Harvard-Smithsonian Center for Astrophysics, Cambridge, MA 02138, USA*
[36]*Department of Astronomy/Steward Observatory, 933 North Cherry Avenue, Tucson, AZ 85721-0065, USA*
[37]*Australian Astronomical Optics, Macquarie University, North Ryde, NSW 2113, Australia*
[38]*Sydney Institute for Astronomy, School of Physics, A28, The University of Sydney, Sydney, NSW 2006, Australia*
[39]*Departamento de Física Matemática, Instituto de Física, Universidade de São Paulo, CP 66318, São Paulo, SP 05314-970, Brazil*
[40]*Observatório Nacional, Rua Gal. José Cristino 77, Rio de Janeiro, RJ 20921-400, Brazil*
[41]*Institució Catalana de Recerca i Estudis Avançats, E-08010 Barcelona, Spain*
[42]*Department of Astrophysical Sciences, Princeton University, Peyton Hall, Princeton, NJ 08544, USA*
[43]*Department of Physics and Astronomy, University of Sussex, Pevensey Building, Brighton BN1 9QH, UK*
[44]*Cerro Tololo Inter-American Observatory, National Optical Astronomy Observatory, Casilla 603, La Serena, Chile*
[45]*Physics Department, Brandeis University, 415 South Street, Waltham, MA 02453, USA*
[46]*Instituto de Física Gleb Wataghin, Universidade Estadual de Campinas, 13083-859 Campinas, SP, Brazil*
[47]*Computer Science and Mathematics Division, Oak Ridge National Laboratory, Oak Ridge, TN 37831, USA*
[48]*Observatories of the Carnegie Institution for Science, 813 Santa Barbara St., Pasadena, CA 91101, USA*

This paper has been typeset from a TEX/LATEX file prepared by the author.